communications
materials

ARTICLE

https://doi.org/10.1038/s43246-023-00388-x OPEN

Imaging Fermi-level hysteresis in nanoscale bubbles of few-layer MoS_2

Dohyeon Jeon[1], Haesol Kim[1], Minji Gu[1] & Taekyeong Kim[1✉]

The electrical stability and reliability of two-dimensional (2D) crystal-based devices are mainly determined by charge traps in the device defects. Although nanobubble structures as defect sources in 2D materials strongly affect the device performance, the local charge-trapping behaviors in nanobubbles are poorly understood. Here, we report a Fermi-level hysteresis imaging strategy using Kelvin probe force microscopy to study the origins of charge trapping in nanobubbles of MoS_2 on SiO_2. We observe that the Fermi-level hysteresis is larger in nanobubbles than in flat regions and increases with the height in a nanobubble, in agreement with our oxide trap band model. We also perform the local transfer curve measurements on the nanobubble structures of MoS_2 on SiO_2, which exhibit enhanced current-hysteresis windows and reliable programming/erasing operations. Our results provide fundamental knowledge on the local charge-trapping mechanism in nanobubbles, and the capability to directly image hysteresis can be powerful tool for the development of 2D material-based memory devices.

---

[1] Department of Physics, Memory and Catalyst Research Center, Hankuk University of Foreign Studies, Yongin 17035, Republic of Korea. ✉email: tkim@hufs.ac.kr

Transition-metal dichalcogenides (TMDCs) have emerged as plausible candidates for the next-generation two-dimensional (2D) semiconducting materials in novel electronic and optoelectronic applications[1,2]. Among such materials, MoS_2 has recently attracted a great deal of attention for thin-film transistors, photodetectors, light-emitting diodes, memory devices, and sensors of various types, due to its high on/off ratio, tunable band gaps, and excellent photoelectric properties[3–6]. Charge traps, which are common in MoS_2 FETs with SiO_2 gate dielectrics and which mostly originate from adsorbates on MoS_2 or SiO_2, defects in MoS_2 or at the MoS_2/SiO_2 interface, and from the insulator material itself, have a considerable effect on the device characteristics[7–11]. For example, defects from sulfur (S) vacancies in MoS_2 and oxide dangling bonds at the MoS_2/SiO_2 interface can degrade the mobility and affect the subthreshold swing (SS) of devices due to the fast charge exchange between the defects and channel[7,12]. Oxide traps known as border traps are located in the SiO_2 within a few nanometers from the interface and exchange charges with the MoS_2 channel through a tunneling process[12–15]. These oxide traps, which have widely distributed time constants depending on their distance from the interface, cause threshold voltage (V_{th}) instability issues such as flicker ($1/f$) noise, hysteresis, and a slowly recoverable V_{th} under gate bias stress[7,16]. In particular, hysteresis, one of the most common phenomena, involves a V_{th} shift under gate voltage (V_G) sweeping in MoS_2/SiO_2 FETs and depends on the energetic alignment of the active oxide traps with the Fermi-level (E_F) of MoS_2[17,18]. It is widely accepted that charge redistributions such as charging and discharging in the acceptor-type defect band of the oxide trap during the V_G sweep process are responsible for the hysteresis in MoS_2/SiO_2 FETs[19,20].

Many researchers have recently studied the nature of traps and their charge-trapping mechanisms through the hysteric behavior in the gate-transfer characteristics of MoS_2/SiO_2 FETs and have made efforts to improve device stability and reliability levels by minimizing the hysteresis[21,22]. However, the observed hysteresis stems from the average response of a large number of charge traps in MoS_2-based devices, which makes it difficult to understand the fundamental properties of individual or local charge traps. Accordingly, probing the hysteresis at the nanoscale spatial resolution is crucial for a complete understanding of the microscopic trap properties and to improve the performance of MoS_2-based devices with inhomogeneous and local charge traps[23].

On the other hand, the formation of inhomogeneous nanobubbles is inevitable between the MoS_2 and the target substrate during the mechanical exfoliation process of MoS_2 onto the substrate. Adsorbed ambient molecules such as liquid water and hydrocarbons become trapped in nanobubbles owing to the van der Waals (vdW) attraction force between the MoS_2 and the substrate[24–27]. Consequently, the MoS_2-based device performance and properties are largely affected by nanobubbles filled with these contaminants. While the nanobubbles usually cause significant degrees of charge inhomogeneity, suppressed carrier mobility, and hysteresis as detrimental to a device, it has been recently reported that liquid water (H_2O) molecules trapped in nanobubbles enhance the charge carrier tunneling through the hexagonal boron nitride (hBN) of the insulating layers from MoS_2 to multilayer graphene (MLG), giving rise to positive effects on the floating gate memory device performance[28]. The nanobubbles and the contaminants trapped inside act as local sources of charge trapping and affect the characteristics of MoS_2-based devices in a variety of ways; however, the origins and mechanisms of the charge trapping occurring in nanobubbles are still not fully understood, especially on the nanoscale.

Herein, we realize a spatially resolved E_F-hysteresis imaging strategy to study localized trap sources in nanobubbles of few-layer MoS_2 on Si/SiO_2. Using Kelvin probe force microscopy (KPFM), we record the E_F-hysteresis curve of MoS_2 by fixing a conductive tip at a desired location and measuring the E_F shift while sweeping V_G, which tunes the occupation of the oxide trap by moving the trap levels across the MoS_2 E_F. The E_F-hysteresis image is obtained by collecting the E_F-hysteresis curve at each tip point in the scan. The measured E_F-hysteresis is larger in a nanobubble than in a flat region because band bending in the dielectric layer due to the trapped H_2O molecules in the nanobubble is added to the oxide trap band bending downward at positive V_G, leading to an increase in the number of occupied oxide traps below the MoS_2 E_F. The nonlinear increase of E_F-hysteresis with the height in a nanobubble is well described by the oxide trap band model with different thicknesses of the H_2O dielectric layers. The energy-distributed trap densities are extracted from the measured E_F-hysteresis curves of the nanobubble and are found also to be consistent with the calculation results based on the oxide trap band model with different thicknesses of the H_2O dielectric layers. Moreover, we perform local gate-transfer measurements using conductive atomic force microscopy (C-AFM), where the enlarged memory windows and stable endurance properties with programming/erasing pulses are achieved in nanobubbles. Our capability to image of E_F-hysteresis should be a significant breakthrough in the fundamental study of localized charge traps and future applications of memory devices based on atomically thin 2D materials.

Results and discussion

E_F-hysteresis imaging on the nanobubbles in MoS_2. Figure 1a shows a schematic diagram of the imaging of E_F-hysteresis of a few-layer MoS_2 on a SiO_2/Si substrate. KPFM is employed to measure the contact potential difference (V_{CPD}) between the KPFM tip and the surface of the MoS_2 in a dry nitrogen (N_2) environment at room temperature. In general, V_{CPD} between the KPFM tip and MoS_2 is defined as $eV_{CPD} = W_{tip} - W_{MoS_2}$, where W_{tip} and W_{MoS_2} denote the work functions of the KPFM tip and MoS_2, respectively[29]. V_G applied to the highly doped Si (p++) substrate controls the carrier density and E_F of the MoS_2 while also modulating W_{MoS_2}. KPFM probes the change of the V_{CPD} (V_G) as determined by the V_G-modulated W_{MoS_2} which corresponds to the E_F variation under the V_G sweep. In this sense, the E_F-hysteresis curve can be obtained from $V_{CPD}(V_G)$ spectrum measurements in the few-layer MoS_2 on a SiO_2/Si substrate during the V_G sweep. To image the E_F-hysteresis of the MoS_2 on SiO_2/Si, the tip is fixed at a specific location and the E_F-hysteresis curve at each point is measured while the sweeping V_G. The spatial map of the E_F-hysteresis is recorded as the sample is raster-scanned (see the "Methods" section for details).

Figure 1b shows a topography image of a few-layer MoS_2 flake prepared by mechanical exfoliation on a Si substrate covered with 300-nm-thick SiO_2. The thickness of MoS_2 is 2.2 nm which corresponds to three layers, as confirmed by the topography image and Raman spectroscopy (see Supplementary Fig. 1). Nanobubbles with heights of ~2–10 nm and flat regions are observed in the topography image. The vdW attraction force between MoS_2 and SiO_2/Si substrate squeezes out the trapped contaminants to the nanobubbles during the transfer of MoS_2, leaving the nanobubbles and the atomically flat regions free of contaminants in the topography image.

Figure 1c contrasts the E_F-hysteresis curves measured on a flat region (red) and a nanobubble with a height of ~8 nm (blue) of few-layer MoS_2 on a SiO_2/Si substrate when V_G is swept from −35 to 10 V (forward) and back to −35 V (backward) at a sweep rate of 0.16 Hz. After acquiring each E_F-hysteresis curve, V_G is set to −35 V for a few seconds to ensure that the MoS_2 recovers fully

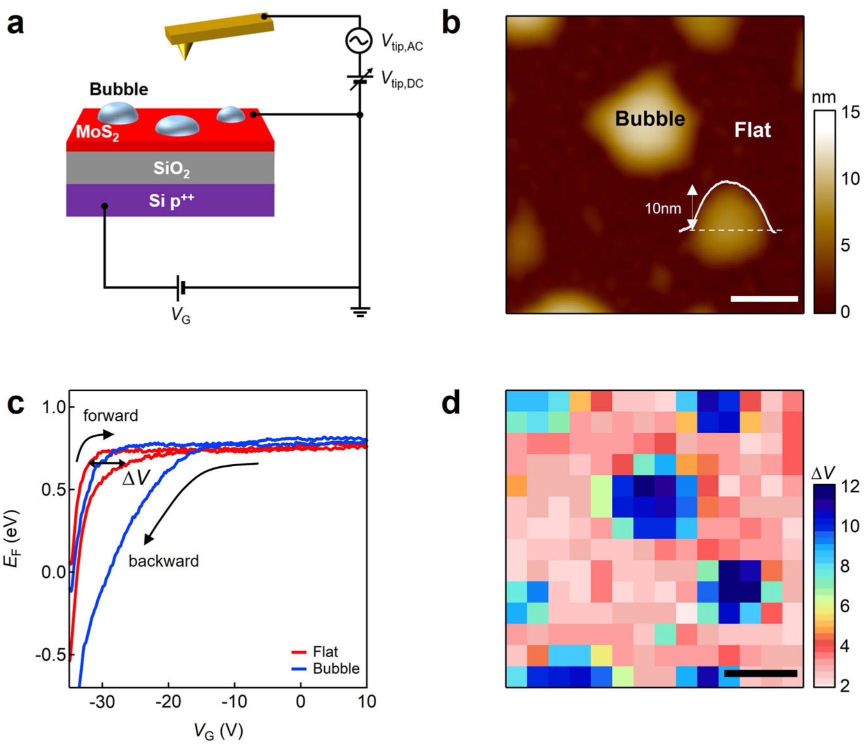

Fig. 1 E_F-hysteresis imaging of few-layered MoS_2 on a SiO_2/Si substrate. a Schematic diagram of E_F-hysteresis imaging via KPFM with external V_G sweeps. **b** AFM topography image; the Inset is the height profile of a nanobubble. **c** E_F-hysteresis curves measured on a flat (red) and a nanobubble (blue) region with a peak height of 8 nm. The E_F-hysteresis width (ΔV) taken at $E_F = 0.65$ eV is larger for a nanobubble than for a flat region, as indicated by the horizontal arrows. **d** A spatially resolved ΔV image obtained via 20 × 20 grid E_F-hysteresis curves on the same topography image region in (**b**). A clear difference is observed between the flat and the nanobubble regions. V_G is swept from −35 to 10 V and back to −35 V at a sweep rate of 0.16 Hz for the E_F-hysteresis curve in each pixel. All scale bars are 0.3 µm.

from the previous V_G stress. The unscreened electric field from the back gate in the bare SiO_2 region can affect V_{CPD} due to the long-range electrostatic interaction between the conducting cantilever and the back gate during the V_G sweep process. Because the surface potential of an Au metal electrode is not affected by V_G due to the high density of states near the Fermi energy of Au metal, the background signal measured on the Au electrode is used to separate the unscreened signals from the V_{CPD} of MoS_2 on the SiO_2/Si substrate[30–32] (see Supplementary Fig. 2). We extract the E_F-hysteresis width (ΔV), referring to the V_{th} shift during the V_G sweep, at a certain E_F corresponding to V_{th}, which is defined as the voltage with the highest curvature of E_F-hysteresis in a forward sweep, as shown by the horizontal arrows[33]. The measured ΔV is 13 V for a nanobubble and 5.5 V for a flat region, measured at an E_F level of 0.65 eV for both the nanobubble and the flat regions. Note that the E_F linearly follows V_G under −30 V in a backward sweep for both the nanobubble and the flat regions, possibly due to the reduced electron carriers and unscreened V_G in the depleted MoS_2[34,35]. The E_F saturation in the E_F-hysteresis curves, which implies E_F pinning near the conduction band edge (E_C), is attributed to the high concentration of electrons owing to the injection from a ground electrode and the amount of S vacancies of MoS_2[19,36].

Figure 1d shows the spatially resolved ΔV map, that is, the E_F-hysteresis image taken at an E_F of 0.65 eV over the same area shown in Fig. 1b. The larger ΔV_s in the nanobubbles compared to the flat regions are clearly resolved in the E_F-hysteresis image. These results imply that nanobubbles with trapped contaminants act as charge-trapping/detrapping spots to cause enlarged E_F-hysteresis in nanobubbles of few-layer MoS_2 on a SiO_2/Si substrate.

Charge trap sources causing the hysteresis. Various trap sources to induce the hysteresis have been suggested in the MoS_2-based FET devices on SiO_2/Si substrates, and these remain a topic of debate[37]. One of the trap sources could be adsorbates such as moisture (H_2O) and oxygen (O_2) molecules on the MoS_2 surface, exchanging charges with the MoS_2 channel and, leading to hysteresis in MoS_2 FETs[8,38]. However, H_2O and O_2 molecules adsorb uniformly on the entire MoS_2 surface rather than only on the nanobubbles. Furthermore, we annealed the MoS_2 sample at 300 °C for one hour before the measurements and obtain E_F-hysteresis imaging during the V_G sweeps in dry N_2 condition (see the “Methods” section), most likely removing most of the surface adsorbates on the MoS_2. Thus, we exclude the surface adsorbates from the charge-trap sources that cause the enlarged E_F-hysteresis in the nanobubbles. The other trap sources could be defects from S vacancies in MoS_2 and/or oxide dangling bonds at the MoS_2/SiO_2 interface[39,40]. However, it has been reported that these defects exchange charges with the MoS_2 channel very rapidly, degrading the mobility due to the scattering at the defects and affecting the subthreshold swing (SS), rather than causing hysteresis in MoS_2 FETs[7,12,17,41]. Furthermore, because the interface trap levels from these defects are distributed inside the band gap, there are no charge-trapping events at these interface states above V_G, where E_F is pinned to E_C[19]. Thus, the charge-trapping process in the interface states would not explain the maximum positive V_G ($V_{G,max}$)-dependence observed in our E_F-hysteresis which increases with $V_{G,max}$, even after E_F is pinned to the E_C for both flat and nanobubble regions (see below and Supplementary Fig. 3). For this reason, we conclude that the interface traps resulting from these defects are not the main source of the E_F-hysteresis in nanobubbles of MoS_2. Another trap source candidate that may cause hysteresis in MoS_2 FETs is SiO_2-bound H_2O molecules between the MoS_2 and SiO_2 substrate[42,43]. The vdW interaction between MoS_2 and the substrate during the exfoliation process squeezes out the H_2O and hydrocarbon molecules into the nanobubbles and leaves flat regions free of contaminants[24–26]. This suggests that the silanol (Si–OH) groups on the SiO_2 surface in the nanobubble regions as compared with those in the flat regions can be more frequently exposed to the trapped H_2O molecules. The silanol groups, which form hydrogen bonds with the trapped H_2O molecules in nanobubbles, could be the source of the charge traps and may partially contribute to the enlarged E_F-hysteresis in nanobubbles (Supplementary Note 1)[40,42,44]. However, because only the bottom layer of H_2O molecules trapped in the nanobubbles can bind to silanol groups on the SiO_2 surface and create a trap sites[44], the contribution from these traps to the E_F-hysteresis in a nanobubble should be constant regardless of the height of a nanobubble, which is not consistent with our experimental results of height-dependent E_F-hysteresis in a nanobubble, as shown below. Therefore, we do not consider SiO_2-bound H_2O molecules as the main trap sources for the larger E_F-hysteresis in the nanobubbles.

To check whether trapped H_2O molecules cause the enlarged E_F-hysteresis in nanobubbles, we performed E_F-hysteresis imaging of MoS_2 on hBN as an insulating layer instead of SiO_2 but found no noticeable difference in the E_F-hysteresis between the flat and nanobubble regions (see Supplementary Figs. 4, 5). These control experiments confirm that we can rule out the trapped H_2O molecules themselves and the induced strains in the nanobubble structure from the sources of charge traps for the enlarged E_F-hysteresis observed in the nanobubbles of MoS_2 on SiO_2/Si.

In other to elucidate the origin of the enlarged E_F-hysteresis in nanobubbles, we calculate the energy band diagrams of MoS_2 on a SiO_2/Si substrate under various V_G conditions based on self-consistently solved Poisson and Schrodinger equations (Supplementary Note 2).

Energy band diagrams with oxide trap band. Figure 2a shows the energy band diagrams of the cross-section of the flat (left) and the nanobubble (right) structures. The oxide traps are energetically localized within the band of the SiO_2 insulator, as indicated by the open circles. We have two oxide trap bands with a simple Gaussian shape depending on the energy[45], located at $E = 2.75$ eV and at $E = 4.56$ eV below the SiO_2 E_C, as reported in the literature based on conventional Si technologies[12,17,18]. The lower oxide trap band is located near the MoS_2 valence band edge (E_V) and does not have a considerable impact on the hysteresis in MoS_2 FETs because the E_F of MoS_2 shifts in the upper half of the band gap during the V_G sweeps process[19]. Therefore, we only consider the upper oxide trap band for the charge trapping and E_F-hysteresis. The upper oxide trap band is assumed to be an acceptor-type trap that is negatively charged below the E_F and neutral above the E_F of MoS_2[7]. Given that the oxide traps exchange the charge with the MoS_2 channel through the tunneling process, these traps should be located within a few nanometers from the MoS_2/SiO_2 interface[7,17]. We use $d_{ox} = 2$ nm as the maximum distance of the active oxide traps from the interface[17,19]. It is well known that H_2O and hydrocarbon molecules are trapped in nanobubbles that form inevitably during the MoS_2 stacking process. We simply assume that 100% of the H_2O or hydrocarbon molecules are trapped in the nanobubble[28], leading to an additional dielectric layer between the MoS_2 and SiO_2 in the energy bands of the nanobubble. A 4-nm-thick of H_2O layer is used for the band diagram of the nanobubble as an example. The parameters for the band gap and electron affinity of MoS_2, SiO_2, and the H_2O layer are shown in Supplementary Table 1. The charge trapping of the flat and nanobubble regions is determined by the energetic alignment of the oxide trap bands relative to the MoS_2 band edges during the V_G sweep process, leading to E_F-hysteresis. For $V_G = -35$ V, most of the oxide traps are above the E_F of MoS_2 and become neutral for the flat and nanobubble regions. For $V_G = 10$ V, the E_F of MoS_2 shifts such that is close to the E_C and the oxide trap bands are bent downward, resulting in charge trapping and occupation in the oxide traps. The number of negatively charged oxide traps below E_F at $V_G = 10$ V is higher for the nanobubble than for the flat region owing to the additional band bending in the H_2O dielectric layer[46–49], which is responsible for the enlarged E_F-hysteresis in nanobubbles. The increased charge exchange between the oxide traps and the MoS_2 channel owing to the H_2O molecules trapped in the nanobubble is also consistent with recent studies which found that H_2O molecules trapped in bubbles enhance the charge carrier tunneling through hBN from MoS_2 to MLG and increase the storage capacities of memory devices[28].

Figure 2b shows the energy-level shifts of the upper band of the oxide trap at $d_{ox} = 2$ nm, denoted by the triangles, as a function of V_G for flat (red) and nanobubble (blue) regions. The energy-level shifts of the upper band of the oxide trap as a function of V_G for the nanobubble with other thicknesses of H_2O layers are shown in Supplementary Fig. 6. The range of the energy-level shifts when sweeping V_G from −35 to 10 V is wider for the nanobubble (~1.6 eV) than for the flat region (~0.4 eV), as indicated by the arrows. This allows a larger number of oxide traps in the nanobubble to participate in the charge-trapping/detrapping events during the V_G sweeps, resulting in the enlarged E_F-hysteresis. In order to investigate the V_G sweep range effect on charge trapping in the oxide traps, we perform the $V_{G,max}$-dependent E_F-hysteresis measurements. Figure 2c shows the measured (empty circles) and calculated (solid lines) ΔV_s as a function of $V_{G,max}$ during the V_G sweep process for the flat (red) and the nanobubble (blue) regions with a peak height of ~4 nm. The measured E_F-hysteresis curves and the calculation details for all $V_{G,max}$ values are shown in Supplementary Figs. 3, 7, respectively. The measured ΔV increases with $V_{G,max}$ even after E_F pinning to E_C at a V_G of −20 V for the flat and nanobubble regions (see Supplementary Fig. 3), in good agreement with the calculated ΔV_s (lines). It should be noted that the high electron concentration in MoS_2 allows E_F to remain pinned to the E_C once E_F advances to E_C as V_G increases. Therefore, the charge-trapping events from the interface traps of which energy levels are inside the band gap of MoS_2 no longer occur after E_F pinning as V_G increases, as reported previously[19]. However, charge-trapping events in oxide traps can increase even after E_F pinning owing to the downward band bending of the oxide traps, which describes well our ΔV_s results for the flat (red) and the nanobubble (blue) regions in Fig. 2c[12,17,19,50].

Height-dependent E_F-hysteresis observed in nanobubbles. Based on this understanding of the energy band diagrams with the oxide traps, we will characterize quantitatively the dependence of E_F-hysteresis on the height of a nanobubble. Figure 3a shows a high-resolution image of E_F-hysteresis, that is, a ΔV image of a single nanobubble, where ΔV is measured at an E_F of 0.65 eV. The inset is the corresponding topography image of the nanobubble, showing a peak height of 8.5 nm. We observe a non-uniform ΔV by obtaining spatially resolved E_F-hysteresis curves of the nanobubble, where the maximum ΔV occurs at its apex. Figure 3b exhibits four distinct E_F-hysteresis curves measured on flat and nanobubble regions with different heights of 1.8, 4, and 6.7 nm of the nanobubble, as denoted by the circles in Fig. 3a.

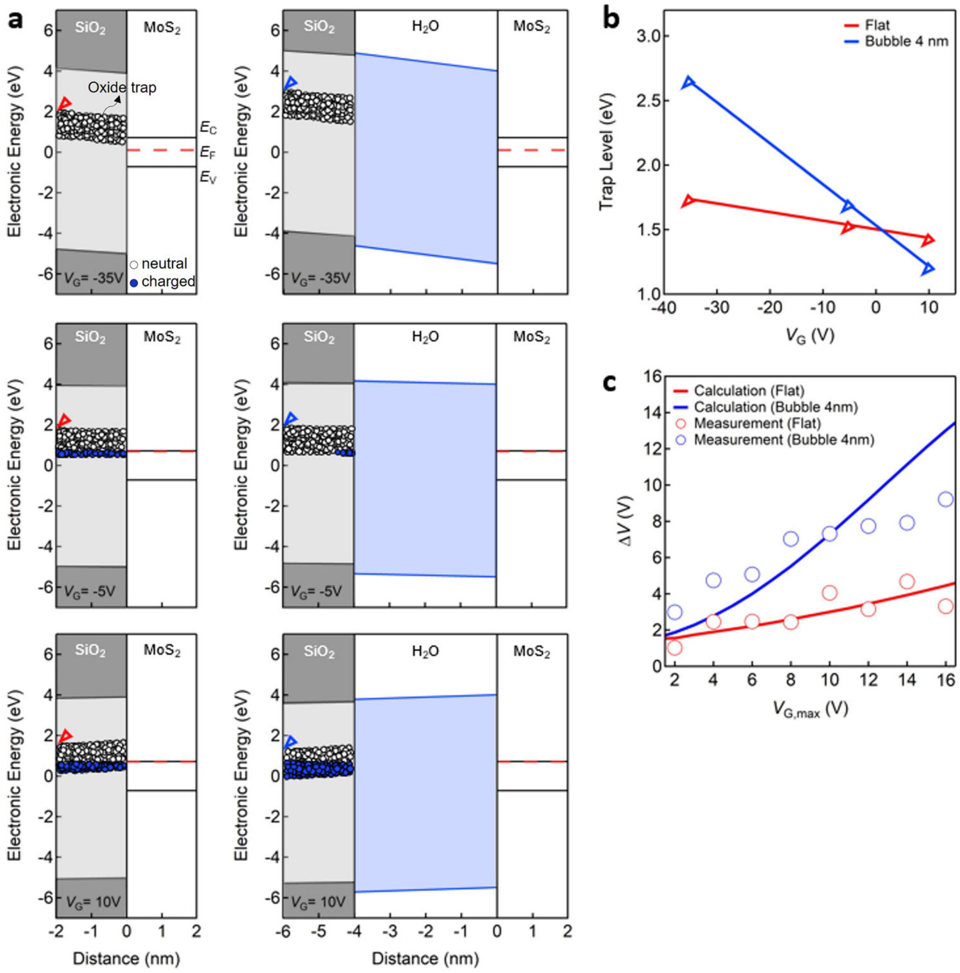

Fig. 2 Energy band diagrams, energy-level shifts, and ΔV variations for a flat and a nanobubble region under various V_G conditions. **a** Energy band diagrams of the cross-sections of a flat (left) and a nanobubble (right) region with a H_2O dielectric layer of 4 nm, and oxide trap level alignments when $V_G = -35$, -5, and 10 V. **b** Energy-level shifts of the upper band of oxide trap at $d_{ox} = 2$ nm for a flat (red) and a nanobubble (blue) region, as indicated by the arrows. **c** Experimentally measured (circles) and calculated (solid curves) ΔV as a function of the positive maximum gate voltage ($V_{G,max}$) under V_G sweeps for flat (red) and nanobubble (blue) regions. These outcomes are in good agreement, and the values increase even after E_F is pinned near E_C at $V_{G,max} = 2$ V, as shown in Supplementary Fig. 7.

This figure clearly shows that the regions with higher heights correspond to larger ΔV values in the E_F-hysteresis image and curves of the nanobubble.

In order to explain the height-dependent E_F-hysteresis of a nanobubble, we utilize the thickness variation of the H_2O layers in the energy band diagrams based on the background, as discussed in Fig. 2a. Figure 3c shows the energy band diagrams at $V_G = 10$ V when the thickness of the H_2O layer 1 nm (left) and 4.5 nm (right) thicknesses of H_2O layers. Here, E_F is close to E_C due to the E_F pinning effect for both thicknesses; however, V_G of 10 V causes a larger number of oxide traps below E_F in the thick (4.5 nm) than in the thin (1 nm) H_2O layer owing to the elongated downward band bending in the thick H_2O layer. This leads to a larger number of occupied oxide traps and a larger ΔV in the thick compared to the thin H_2O layer in a nanobubble. To observe the height-dependent behavior of E_F-hysteresis in a single nanobubble, we plot ΔV as a function of the height of a nanobubble in Fig. 3d. The circles are experimental results extracted from the E_F-hysteresis and the corresponding topography image in Fig. 3a, and the solid line is the calculation results based on the energy band diagrams with different thicknesses of H_2O layers (see Supplementary Note 3). The nonlinear dependency of ΔV on the height is observed in the nanobubble region for both the calculation and the experimental results. This is attributed to the nonlinear increase of the oxide traps below the E_F of MoS_2 at $V_G = 10$ V when the thickness of the H_2O layer increases from 1 nm to 8 nm. The calculated ΔV is in good agreement with the experimentally measured ΔV for the nanobubble, which confirms that our oxide trap band model with H_2O layers suitably describes the height-dependent E_F-hysteresis observed in nanobubbles.

Energy-distributed trap density extraction. To further confirm that the E_F-hysteresis in a nanobubble originates from oxide traps, we extract the energy-distributed trap densities (D_T) from the measured E_F-hysteresis curves and compare them to the calculated D_T based on the oxide trap band model. The capacitor network model (CNM)[15,41] is employed to extract D_T from the experimentally measured E_F-hysteresis curves in the flat and nanobubble regions. Figure 4a shows an illustration of the CNM of flat (left) and nanobubble (right) structures, where C_Q and C_{OX} are the quantum capacitance and the SiO_2 capacitance, respectively. C_T is the capacitance owing to the oxide traps and C_{H_2O} is the capacitance owing to the H_2O dielectric layer in the nanobubble. V_{CH} denotes the voltage drop in the MoS_2 channel; that

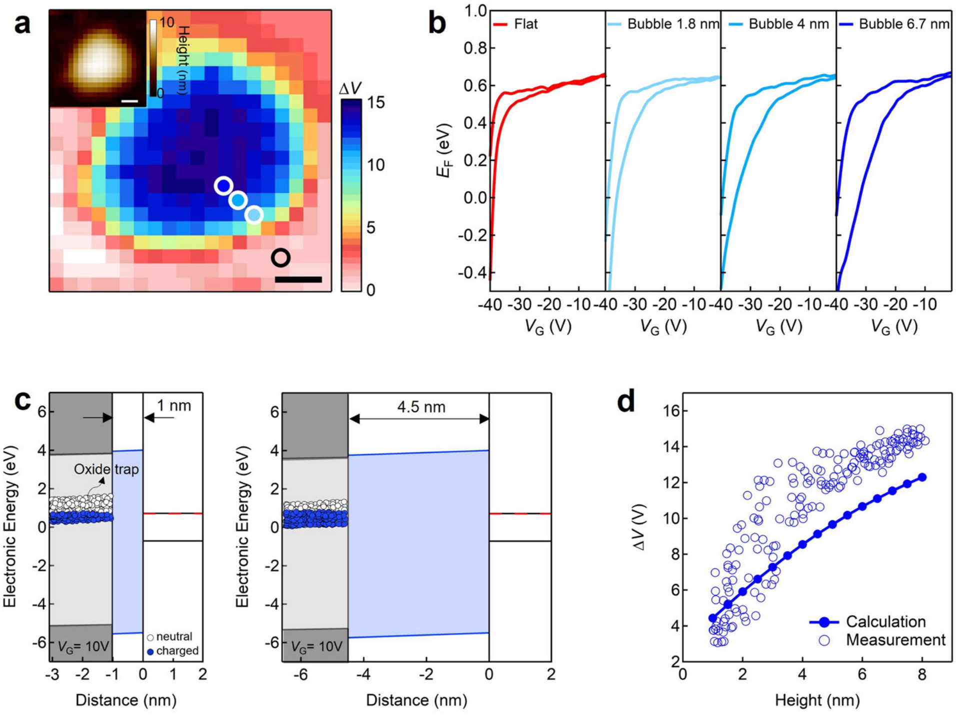

Fig. 3 Height dependence of E_F-hysteresis in a nanobubble. a High-resolution ΔV image (taken at $E_F = 0.65$ eV) of a single nanobubble, where the inset is an AFM topography image of a nanobubble with a peak height of 8.5 nm. Scale bars, 0.1 µm. **b** Sample E_F-hysteresis curves from the corresponding points indicated by circles on flat and nanobubble regions (1.8, 4, and 6.7 nm) in **a**. Here, V_G is swept from −40 to 10 V and back to −40 V at a sweep rate of 0.16 Hz for all of the E_F-hysteresis curve measurements. **c** Energy band diagram of the nanobubble with 1 nm (left) and 4.5 nm (right) H_2O dielectric layers under V_G of 10 V. The number of oxide traps below E_F is larger for the 4.5 nm H_2O layer as compared to the 1 nm H_2O layer, which is attributed to the elongated band bending in the downward direction at a positive V_G in the 4.5 nm H_2O layer, leading to the larger E_F-hysteresis at a higher position in the nanobubble. **d** Experimentally measured ΔV (circles) and calculated ΔV (line) values as a function of the height of a nanobubble.

is, $V_{CH} = E_F/q$. Based on the CNM, D_T is derived as follows:

$$D_T = \frac{1}{q} C_T = \frac{C_{ox}}{q}\left(\frac{dV_G}{dV_{CH}} - 1\right) - C_Q \qquad (1)$$

where $\frac{dV_G}{dV_{CH}}$ is extracted from the backward sweep of the experimentally measured E_F-hysteresis curve[35,36,51,52]. Figure 4b shows the backward E_F-hysteresis curves measured on the flat (red) and the nanobubble (blue series) regions with different heights of 1.8, 4, and 6.7 nm, as presented in Fig. 3b. The lines in Fig. 4c are the calculated backward E_F-hysteresis curves based on the oxide trap band model (see Supplementary Fig. 8 for the calculation details), indicating excellent agreement with the measured values for flat and nanobubble regions. Figure 4d shows D_T extracted from the backward E_F-hysteresis curves on the flat (red circle) and the nanobubble (blue series circles) regions, as shown in Fig. 3a. A higher height in the nanobubble shows a larger D_T in most energy ranges, consistent with the height dependent ΔV results, i.e., larger downward band bending and more charge-trapping events in the thicker H_2O layer. The extracted D_T is in the same range of 10^{12}–10^{13} cm^{-2} eV^{-1} in the oxide trap densities of the SiO_2 insulating layer as reported in the literature[12,53,54]. D_T increases with the energy; that is, it increases from the depletion to the accumulation range and shows a maximum near E_C of MoS_2 for both flat and nanobubble regions, in accordance with earlier results pertaining to energy-distributed border traps in oxide insulating layers[15,55]. The lines in Fig. 4e are the calculated D_T obtained from the oxide trap band model, which is in good agreement with the extracted D_T from the experimentally measured E_F-hysteresis curves for flat and nanobubble regions, although additional small peaks in the measured cases, presumably associated with traps induced by the silanol-group (Si–OH)-bound H_2O molecules in a nanobubble, are present. These results further confirm that the oxide traps are the origin of our E_F-hysteresis, and the oxide trap band model is essential to elucidate the E_F-hysteresis of nanobubble structures.

It should be noted that the CNM does not consider the time constants of the traps, however, the oxide traps as border traps have the widely distributed time constants depending on the distance from the MoS_2 channel interface[7,17]. Therefore, information about the time constants of the oxide traps is required to obtain a more accurate D_T from the E_F-hysteresis. The effects of the time constants on E_F-hysteresis increase for thicker rather than thin H_2O layers in nanobubble structures. For example, the measured backward E_F-hysteresis curves (blue series) on thin (1.8 nm) and thick (8.2 nm) positions in a nanobubble show different behaviors in a V_G range of about −20 to −35 V, where E_F decreases more steeply for thick than for thin positions, as shown in Fig. 4f. These different behaviors are presumably attributed to the longer emission time constant (τ_e) resulting from the reduced tunneling from oxide traps to the MoS_2 channel with the thicker H_2O layer. Once V_G approaches $V_{G,max}$ in the forward V_G sweep, all traps below E_F are assumed to be occupied by electrons; they, start to emit electrons above E_F into the MoS_2 channel and become neutral (i.e., unoccupied) depending on their τ_e during the backward V_G sweep[17,56]. Because the occupied electrons remain in oxide traps above E_F owing to the longer τ_e for a thicker H_2O layer region and can affect the backward E_F-hysteresis curve during the backward V_G sweep, the thick H_2O region has a larger E_F drop than the thin H_2O region for the same negative V_G. In other to prove the τ_e effects on the E_F-hysteresis curves, we calculated backward

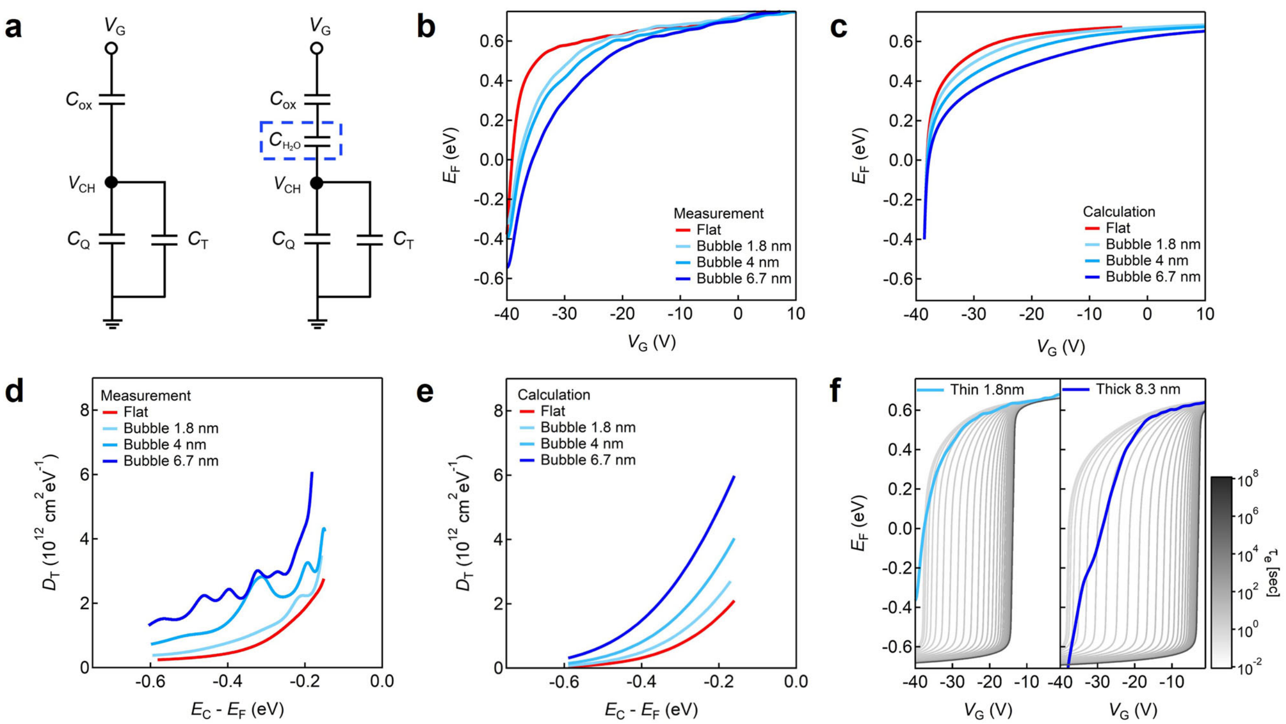

Fig. 4 Comparison of experimentally extracted and calculated D_T in a nanobubble region. a Illustration of the capacitor network model (CNM) for the flat (left) and nanobubble (right) regions, where C_{H_2O} is the capacitance owing to the H_2O layer in the nanobubble. C_Q and C_{OX} are the quantum capacitance and the SiO_2 capacitance, respectively. **b** Measured backward E_F hysteresis curves on flat (red series) and nanobubble (blue series) regions with different heights of 1.8, 4, and 6.7 nm. **c** Calculated backward E_F-hysteresis curves based on the oxide trap band model. **d** Energy-distributed D_T extracted from the measured backward E_F-hysteresis curves of flat (red series) and nanobubble regions (blue series) with different heights of 1.8, 4, and 6.7 nm. **e** Calculated D_T of flat (red series) and nanobubble regions (blue series) using CNM. **f** Measured backward E_F-hysteresis curves for nanobubble with heights of 1.8 nm (left) and 8.2 nm (right). The lines are the calculated backward E_F-hysteresis curves on nanobubble with an H_2O layer with thicknesses of 1.8 nm (left) and 8.2 nm (right), where τ_e in the range of 10^{-1}–10^8 s is used for the calculation.

E_F-hysteresis curves (gray series) for nanobubbles with H_2O layer thicknesses of 1.8 nm (left) and 8.2 nm (right) while varying τ_e, as shown in Fig. 4f (see Supplementary Fig. 8 for the calculation details). These results show that a longer τ_e is required to generate the backward E_F-hysteresis curve measured on the thick (8.2 nm) H_2O layer, whereas a shorter τ_e is enough to generate the backward E_F-hysteresis curve measured on the thin (1.8 nm) H_2O layer. It confirms that a longer τ_e induces the larger E_F drop during a backward V_G sweep on the thick H_2O layer in nanobubble structures, as shown by the measured backward E_F-hysteresis curves in Fig. 4f.

In the calculation, we use an identical value of τ_e for the entire V_G sweep range; however, the time constants of the oxide traps show a rather large dependence on V_G. The V_G-dependent capture and emission time constants can be obtained using the nonradiative multiphonon (NMP) model[16,17], which feasibly describes charge-trapping events in oxide traps using the structural relaxation at the trap sites, as the main characteristic of the model. A full calculation of the V_G-dependent time constants and the corresponding D_T requires a comprehensive investigation of the NMP model for oxide traps with various H_2O layer thicknesses, which is, however, beyond the scope of the present work.

Non-volatile memory device applications based on the nanobubble structures. In order to demonstrate the feasibility of a MoS_2 nanobubble with a high density of trap states for use in memory device applications, we acquire the transfer curve measurements on the nanobubble using the conductive atomic force microscopy (C-AFM) technique (see the "Methods" section). Figure 5a shows a schematic diagram of the C-AFM for current (I_{DS})-hysteresis curve measurements. The metal-coated tip used here is located at the selected positions of the nanobubble and flat regions, and the I_{DS} under a fixed source–drain voltage (V_{DS}) is measured as V_G is swept from −40 to 10 V and back to −40 V. Figure 5b shows the transfer characteristics, where four I_{DS}–V_G curves at $V_{DS} = 5$ V are measured consecutively on both the flat (red) and the nanobubble (blue) regions. The tip is positioned at the top of the nanobubble which has a peak height of ~10 nm. It should be noted that the separation between the tip contact position and the Au electrode is set to be nearly identical for the flat region and the nanobubble in the I_{DS}–V_G measurements because separation-dependent variations of the number of oxide traps below the channel can affect the I_{DS}-hysteresis. The outcome clearly shows that the I_{DS}-hysteresis is larger for the nanobubble than for the flat region, consistent with our E_F-hysteresis results. This enhanced nonvolatile charge storage capability mainly results from the increased charge-trapping/detrapping events in the nanobubble structure of MoS_2 on the SiO_2 insulator. Cyclic endurance tests are conducted during repeated programming (P)/erasing (E) operations to confirm the reliability of the nanobubble-based memory devices (see Supplementary Fig. 9 for details). Figure 5c plots I_{DS} measured at $V_{DS} = 5$ V under the read state of $V_G = -30$ V with a $V_G = 10$ V pulse for 1 s as the P state and a $V_G = -40$ V pulse for 1 s as the E state on the flat (red) and the nanobubble (blue) positions, exhibiting the stable and reproducible switching performance for more than 1000 cycles. To further investigate the stability of P and E states of the nanobubbles structures, which is crucial for the nonvolatile memory cells, we perform a memory retention

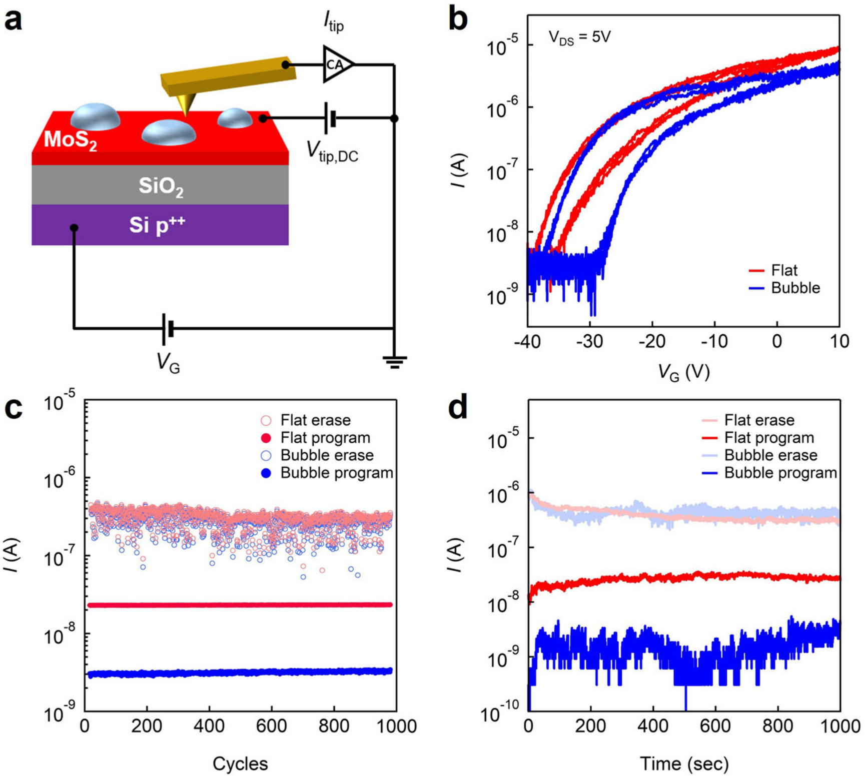

Fig. 5 C-AFM measurements for the I_{DS}-hysteresis and the endurance/retention characteristics of a nanobubble structure. a Schematic diagram of current (I_{DS})-hysteresis curve measurements on nanobubbles from C-AFM. **b** Transfer characteristic on a flat region (red) and a nanobubble (blue) as V_G is swept at a sweep rate of 0.16 Hz, under the applied $V_{DS} = 5$ V. The I_{DS}-hysteresis window is larger for the nanobubble than for the flat region. **c** Endurance performance tests on a flat region (red) and a nanobubble (blue) for 1000 cycles with the programming (10 V, 1 s)/erasing (−40 V, 1 s) pulse operations. **d** Retention performance tests on a flat region (red) and a nanobubble (blue) for 1000 s. The stable *P* and *E* states are observed at $V_{DS} = 5$ V even after 1000 s elapse since *P* (10 V, 1 s)/*E* (−40 V, 1 s) pulses.

test in Fig. 5d. It shows the temporal evolution of I_{DS} measured at $V_{DS} = 5$ V under the read state of $V_G = -30$ V with a $V_G = 10$ V pulse for 1 s as the *P* state and a $V_G = -40$ V pulse for 1 s as the *E* state, respectively. The *P* and *E* states are distinguishable and remained stable for 1000 s on the flat (red) and the nanobubble (blue) positions. It should be noted that the nanobubble retained a nearly identical shape after the transfer measurements and endurance/retention tests (see Supplementary Figs. 10, 11), further confirming that nanobubble structures can be employed for nonvolatile memory and data storage applications.

Conclusion

We demonstrated the local mapping of E_F-hysteresis of few-layer MoS_2 on a SiO_2/Si substrate using KPFM combined with gate sweep operations and observed that the E_F-hysteresis is larger in a nanobubble as compared to a flat region and that it increases nonlinearly with the height of nanobubble. The energy-level alignment of oxide traps with MoS_2 E_F under gate sweeps causes hysteresis in the transfer characteristics of the conventional MoS_2 FETs, whereas the additional downward bending of the oxide trap band in conjunction with the band of the H_2O dielectric layer at a positive V_G leads to an increased number of occupied charge traps below the MoS_2 E_F and enlarged E_F- and I_{DS}-hysteresis in a nanobubble. The trap densities extracted from the measured E_F-hysteresis curves of flat and nanobubble regions are well described by the oxide trap band model, which further confirms that the E_F-hysteresis originates from the oxide traps and our band bending scenario is essential for local charge tapping/detrapping in nanobubble structures. The local measurements of the transfer curves on the nanobubbles, which show the enlarged I_{DS}-hysteresis window and reliable cyclic endurance, are consistent with our E_F-hysteresis results. Our results provide new insight into the charge-trapping process in nanobubbles of MoS_2 on a SiO_2/Si substrate, and the ability to image E_F-hysteresis represents a significant breakthrough in the fundamental study of local charge-trapping sources and practical applications of MoS_2 based nonvolatile memory devices.

Methods

KPFM and C-AFM measurements. All the KPFM and C-AFM measurements based on XE-7 (Park Systems Corp.) were operated in a glove box filled with dry nitrogen at room temperature to avoid unwanted effects caused by O_2 and H_2O molecules. An NSC36/Cr-Au (Mikro Masch) tip with a nominal resonance frequency of 65 kHz and a nominal spring constant of 0.6 N m^{-1} is used for the KPFM measurements. The AC bias voltage of V_{ac} sin(ωt) with a 2 V amplitude and an electrical excitation frequency (ω) of 17 kHz is applied to the tip during the KPFM measurements using an external SR830 lock-in amplifier (Stanford Research Systems Inc.). E_F-hysteresis imaging is performed in an automated spectroscopic mapping mode using the XE-7 with a customized program for precise tip positioning at each spatial location (pixel) of the grid. A data acquisition card (DAQ, PXI-6221, National Instruments) with a custom-made voltage amplifier (LTC 6090 op-amp (max supply voltage ±70 V)) controlled by a custom LabView code FPGA module (PCIe-8361, National Instruments), is employed to apply the external gate voltages to the sample, also collecting the V_{CPD} signals from the AFM via a SAM (Signal Access Module, Park systems) after further filtering the signals with a low-pass filter (SR650, Stanford Research Systems, Inc.). The external gate voltage signals from the DAQ are synchronized with the end-of-pixel TTL (Transistor–Transistor Logic) pulse and applied to each pixel where the tip approaches the sample surface. During the E_F-hysteresis sweeps on each pixel of the grid, the tip is within a distance of 10 nm above the sample surface to avoid topographic artifacts caused by the cantilever amplitude feedback control process. The tip waits for 3–5 s under $V_G = -40$ V before moving to the next pixel to ensure that the MoS_2 fully recovers from the previous gate bias stress.

An NSC18/Cr-Au (Mikro Masch) tip with a nominal resonance frequency of 75 kHz and a nominal spring constant of 2.8 N m^{-1} is used for the C-AFM measurements. The tip is kept grounded and carefully placed on the nanobubbles with a loading force of 10 nN after contact-mode topography imaging. DC bias voltage is applied to the MoS_2 flake via Au thin film for current measurements using a low noise current amplifier (VECA DLPCA-200, FEMTO).

MoS_2 sample fabrication. A MoS_2 flake is exfoliated onto a silicon substrate coated with a 300-nm-thick thermal oxide layer using a mechanical cleavage approach reported previously[57]. Thin Au metal film with a 30 nm thickness as a ground electrode is pre-fabricated on a Si substrate and physically transferred onto one side of the MoS_2 flake using a polydimethylsiloxane (PDMS) stamp under a microscope for proper alignment (optical microscopic image in see Supplementary Fig. 1), allowing us to avoid contamination and defects caused by a conventional lithography and thermal evaporation processes[58,59]. After transferring the Au film, the sample is annealed at 300 °C for 1 h in the N_2 condition before the KPFM and C-AFM measurements to remove the O_2 and H_2O residue from the MoS_2 surface.

Data availability

All data used for analysis is made available upon request to the corresponding author.

Code availability

All code used for analyzing the data is made available upon request to the corresponding author.

Received: 30 December 2022; Accepted: 31 July 2023;

References

1. Akinwande, D. et al. Graphene and two-dimensional materials for silicon technology. *Nature* **573**, 507–518 (2019).
2. Huo, N. & Konstantatos, G. Recent progress and future prospects of 2D-based photodetectors. *Adv. Mater.* **30**, e1801164 (2018).
3. Migliato Marega, G. et al. Logic-in-memory based on an atomically thin semiconductor. *Nature* **587**, 72–77 (2020).
4. Nalwa, H. S. A review of molybdenum disulfide (MoS_2) based photodetectors: from ultra-broadband, self-powered to flexible devices. *RSC Adv.* **10**, 30529–30602 (2020).
5. Jiang, J. et al. Flexo-photovoltaic effect in MoS_2. *Nat. Nanotechnol.* **16**, 894–901 (2021).
6. Manzeli, S., Dumcenco, D., Migliato Marega, G. & Kis, A. Self-sensing, tunable monolayer MoS_2 nanoelectromechanical resonators. *Nat. Commun.* **10**, 4831 (2019).
7. Illarionov, Y. Y. et al. Insulators for 2D nanoelectronics: the gap to bridge. *Nat. Commun.* **11**, 3385 (2020).
8. Li, T., Du, G., Zhang, B. & Zeng, Z. Scaling behavior of hysteresis in multilayer MoS_2 field effect transistors. *Appl. Phys. Lett* **105**, 093107 (2014).
9. Park, Y., Baac, H. W., Heo, J. & Yoo, G. Thermally activated trap charges responsible for hysteresis in multilayer MoS_2 field-effect transistors. *Appl. Phys. Lett* **108**, 083102 (2016).
10. Shu, J. et al. The intrinsic origin of hysteresis in MoS_2 field effect transistors. *Nanoscale* **8**, 3049–3056 (2016).
11. Fang, N., Toyoda, S., Taniguchi, T., Watanabe, K. & Nagashio, K. Full energy spectra of interface state densities for n- and p-type MoS_2 field-effect transistors. *Adv. Funct. Mater.* **29**, 1904465 (2019).
12. Illarionov, Y. Y. et al. Energetic mapping of oxide traps in MoS_2 field-effect transistors. *2D Mater.* **4**, 025108 (2017).
13. Fleetwood, D. M. "Border traps" in MOS devices. *IEEE Trans. Nucl. Sci.* **39**, 269–271 (1992).
14. Illarionov, Y. Y. et al. The role of charge trapping in MoS_2/SiO_2 and $MoS_2/$hBN field-effect transistors. *2D Mater.* **3**, 035004 (2016).
15. Zhao, P. et al. Evaluation of border traps and interface traps in HfO_2/MoS_2 gate stacks by capacitance–voltage analysis. *2D Mater.* **5**, 031002 (2018).
16. Stampfer, B. et al. Characterization of single defects in ultrascaled MoS_2 field-effect transistors. *ACS Nano* **12**, 5368–5375 (2018).
17. Grasser, T. Stochastic charge trapping in oxides: From random telegraph noise to bias temperature instabilities. *Microelectron. Reliab.* **52**, 39–70 (2012).
18. Knobloch, T. et al. Improving stability in two-dimensional transistors with amorphous gate oxides by Fermi-level tuning. *Nat. Electron.* **5**, 356–366 (2022).
19. Knobloch, T. et al. A physical model for the hysteresis in MoS_2 transistors. *IEEE J. Electron Devices Soc.* **6**, 972–978 (2018).
20. Illarionov, Y. Y. et al. Long-term stability and reliability of black phosphorus field-effect transistors. *ACS Nano* **10**, 9543–9549 (2016).
21. Liu, S. et al. Hysteresis-free hexagonal boron nitride encapsulated 2D semiconductor transistors, NMOS and CMOS inverters. *Adv. Electron. Mater.* **5**, 1800419 (2018).
22. Vu, Q. A. et al. Near-zero hysteresis and near-ideal subthreshold swing in h-BN encapsulated single-layer MoS_2 field-effect transistors. *2D Mater.* **5**, 031001 (2018).
23. Rhodes, D., Chae, S. H., Ribeiro-Palau, R. & Hone, J. Disorder in van der Waals heterostructures of 2D materials. *Nat. Mater.* **18**, 541–549 (2019).
24. Sanchez, D. A. Mechanics of spontaneously formed nanoblisters trapped by transferred 2D crystals. *PNAS* **115**, 7884–7889 (2018).
25. Khestanova, E., Guinea, F., Fumagalli, L., Geim, A. K. & Grigorieva, I. V. Universal shape and pressure inside bubbles appearing in van der Waals heterostructures. *Nat. Commun.* **7**, 12587 (2016).
26. Haigh, S. J. et al. Cross-sectional imaging of individual layers and buried interfaces of graphene-based heterostructures and superlattices. *Nat. Mater.* **11**, 764–767 (2012).
27. Darlington, T. P. et al. Imaging strain-localized excitons in nanoscale bubbles of monolayer WSe_2 at room temperature. *Nat. Nanotechnol.* **15**, 854–860 (2020).
28. Gwon, O. H. et al. Systematic design and demonstration of multi-bit generation in layered materials heterostructures floating-gate memory. *Adv. Funct. Mater.* **31**, 2105472 (2021).
29. Melitz, W., Shen, J., Kummel, A. C. & Lee, S. Kelvin probe force microscopy and its application. *Surf. Sci. Rep.* **66**, 1–27 (2011).
30. Yu, Y.-J. et al. Tuning the graphene work function by electric field effect. *Nano Lett* **9**, 3430–3434 (2009).
31. Wang, Z. et al. The ambipolar transport behavior of WSe_2 transistors and its analogue circuits. *NPG Asia Mater.* **10**, 703–712 (2018).
32. Wang, Y. et al. Direct observation of the hysteretic Fermi level modulation in monolayer MoS_2 field effect transistors. *Curr. Appl. Phys.* **20**, 298–303 (2020).
33. Ma, N. & Jena, D. Carrier statistics and quantum capacitance effects on mobility extraction in two-dimensional crystal semiconductor field-effect transistors. *2D Mater.* **2**, 015003 (2015).
34. Dagan, R., Vaknin, Y., Weisman, D., Amit, I. & Rosenwaks, Y. Accurate method to determine the mobility of transition-metal dichalcogenides with incomplete gate screening. *ACS Appl. Mater. Interfaces* **11**, 44406–44412 (2019).
35. Zhang, Y., Ziegler, D. & Salmeron, M. Charge trapping states at the SiO_2-oligothiophene monolayer interface in field effect transistors studied by Kelvin probe force microscopy. *ACS Nano* **7**, 8258–8265 (2013).
36. Dagan, R., Vaknin, Y. & Rosenwaks, Y. Gap state distribution and Fermi level pinning in monolayer to multilayer MoS_2 field effect transistors. *Nanoscale* **12**, 8883–8889 (2020).
37. Arnold, A. J. et al. Mimicking neurotransmitter release in chemical synapses via hysteresis engineering in MoS_2 transistors. *ACS Nano* **11**, 3110–3118 (2017).
38. Late, D. J., Liu, B., Matte, H. S. S. R., Dravid, V. P. & Rao, C. N. R. Hysteresis in single-layer MoS_2 field effect transistors. *ACS Nano* **6**, 5635–5641 (2012).
39. Di Bartolomeo, A. et al. Hysteresis in the transfer characteristics of MoS_2 transistors. *2D Mater.* **5**, 015014 (2018).
40. Guo, Y. et al. Charge trapping at the MoS_2–SiO_2 interface and its effects on the characteristics of MoS_2 metal-oxide-semiconductor field effect transistors. *Appl. Phys. Lett.* **106**, 103109 (2015).
41. Zhu, W. et al. Electronic transport and device prospects of monolayer molybdenum disulphide grown by chemical vapour deposition. *Nat. Commun.* **5**, 3087 (2014).
42. Kim, W. et al. Hysteresis caused by water molecules in carbon nanotube field-effect transistors. *Nano Lett.* **3**, 193–198 (2003).
43. Bartolomeo, A. D. et al. Electrical properties and memory effects of field-effect transistors from networks of single- and double-walled carbon nanotubes. *Nanotechnology* **21**, 115204 (2010).
44. Iqbal, H. F., Waldrip, M., Chen, H., McCulloch, I. & Jurchescu, O. D. Elucidating the role of water-related traps in the operation of polymer field-effect transistors. *Adv. Electron. Mater.* **7**, 2100393 (2021).
45. Schanovsky, F., Gös, W. & Grasser, T. Multiphonon hole trapping from first principles. *J. Vac. Sci. Technol. B: Nanotechnol. Microelectron.* **29**, 01A201 (2011).
46. Tiwari, S. et al. A silicon nanocrystals based memory. *Appl. Phys. Lett.* **68**, 1377–1379 (1996).
47. Chang, T. C. et al. Quasi-superlattice storage. *J. Electrochem. Soc.* **151**, G805 (2004).
48. Lee, S., Seong, H., Im, S. G., Moon, H. & Yoo, S. Organic flash memory on various flexible substrates for foldable and disposable electronics. *Nat. Commun.* **8**, 725 (2017).
49. Chen, W. et al. Multistacked $Al_2O_3/HfO_2/SiO_2$ tunnel layer for high-density nonvolatile memory application. *Appl. Phys. Lett.* **91**, 022908 (2007).

50. Illarionov, Y. Y. et al. Highly-stable black phosphorus field-effect transistors with low density of oxide traps. *npj 2D Mater. Appl.* **1**, 23 (2017).
51. Tal, O. et al. Direct determination of the hole density of states in undoped and doped amorphous organic films with high lateral resolution. *Phys. Rev. Lett.* **95**, 256405 (2005).
52. Yogev, S. et al. Fermi level pinning by gap states in organic semiconductors. *Phys. Rev. Lett.* **110**, 036803 (2013).
53. Li, X. et al. Effect of dielectric interface on the performance of MoS_2 transistors. *ACS Appl. Mater. Interfaces* **9**, 44602–44608 (2017).
54. Renteria, J. et al. Low-frequency 1/f noise in MoS_2 transistors: relative contributions of the channel and contacts. *Appl. Phys. Lett* **104**, 153104 (2014).
55. Zhao, P. et al. Understanding the impact of annealing on interface and border traps in the $Cr/HfO_2/Al_2O_3/MoS_2$ system. *ACS Appl. Electron. Mater.* **1**, 1372–1377 (2019).
56. Grasser T. *Bias Temperature Instability for Devices and Circuits* (Springer Science+Business Media, New York, 2014).
57. Dean, C. R. et al. Boron nitride substrates for high-quality graphene electronics. *Nat. Nanotechnol.* **5**, 722–726 (2010).
58. Liu, Y. et al. Approaching the Schottky–Mott limit in van der Waals metal–semiconductor junctions. *Nature* **557**, 696–700 (2018).
59. Dong, W. J., Kim, S., Park, J. Y., Yu, H. K. & Lee, J.-L. Ultrafast and chemically stable transfer of Au nanomembrane using a water-soluble NaCl sacrificial layer for flexible solar cells. *ACS Appl. Mater. Interfaces* **11**, 30477–30483 (2019).

Acknowledgements

This study was supported by the National Research Foundation of Korea (Grant No. 2022R1F1A106610611) and the Hankuk University of Foreign Studies Research Fund.

Author contributions

D.J. and T.K. conceived the idea of this work. D.J., H.K., and M.G. fabricated the sample. D.J. and M.G. performed the experiments. D.J. and H.K. performed data analysis and calculations. T.K. supervised overall work. This manuscript was written through the contributions of all authors. All authors have given approval to the final version of the manuscript.

Competing interests

The authors declare no competing interests.

Additional information

Supplementary information The online version contains supplementary material available at https://doi.org/10.1038/s43246-023-00388-x.

Correspondence and requests for materials should be addressed to Taekyeong Kim.

Peer review information *Communications Materials* thanks the anonymous reviewers for their contribution to the peer review of this work. Primary Handling Editor: Aldo Isidori. A peer review file is available.